Simulating compressibility in cavitating flows with an incompressible mass transfer flow solver

Schenke, Sören; van Terwisga, Thomas

Publication date
2017

Document Version
Final published version

Published in
Proceedings of the 5th International Symposium on Marine Propulsion (SMP 2017)

Citation (APA)
Schenke, S., & van Terwisga, T. (2017). Simulating compressibility in cavitating flows with an incompressible mass transfer flow solver. In A. Sánchez-Caja (Ed.), *Proceedings of the 5th International Symposium on Marine Propulsion (SMP 2017)* (pp. 71-79). Article MA2.4 VTT Technical Research Centre of Finland.

Fifth International Symposium on Marine Propulsors
smp'17, Espoo, Finland, June 2017

Simulating Compressibility in Cavitating Flows with an Incompressible Mass Transfer Flow Solver

Sören Schenke[1], **Tom J.C. van Terwisga**[1,2]

[1]Department of Ship Hydromechanics & Structures, Delft University of Technology (TUD), Delft, the Netherlands
[2]Maritime Research Institute Netherlands (MARIN), Wageningen, the Netherlands

ABSTRACT

The effect of finite mass transfer rate in combination with temporal resolution on the dynamics of caviting flows is subject of this study. It will be shown that global flow quantities exhibit convergent behaviour with respect to mass transfer rate and time step size in incompressible pressure-based simulation of cavitating flows. It is concluded that large mass transfer rates are required in combination with sufficiently small time steps to focus the local phase transition process to time intervals which are small with respect to both the time scale of the flow (Sezal 2009) and the characteristic cavity collapse time. Koukouvinis & Gavaises (2015) as well as Bhatt et al (2015) came to similar conclusions. The effect of finite mass transfer is demonstrated by numerical studies of an isolated bubble collapse and a cavitating wedge flow. It is further shown how a conventional finite mass transfer approach must be modified to achieve homogeneous equilibrium states as given by an arbitrary barotropic equation of state in the presence of advective density change.

Keywords

Equilibrium flow, equilibrium state, mass transfer, cavitation dynamics

1 INTRODUCTION

The model parameters of finite mass transfer models, typically incorporated in incompressible pressure-based flow solvers, are often considered as empirical (Frikha et al 2008 and Charrière et al 2015). The finite mass transfer approach is referred to as the family of models for which the mass transfer rate is assumed to be related to the amount by which pressure is above or below vapour pressure or similar semi-empirical relations. The magnitude of mass transfer rate is often tunable by the model constants (Charrière et al 2015), but the mass transfer rate required to achieve realistic simulation results are typically unknown. Another family of cavitation models is based on the assumption that the flow variables always exist in well-posed homogeneous equilibrium states as given by simple barotropic equations of state or more advanced thermodynamic considerations.

The characteristic difference in behaviour of both approaches is seen from the evolution of local density-pressure trajectories. In case of the homogeneous equilibrium approach, the trajectory is unique and must always follow the curve given by the equation of state, while in case of the finite mass transfer approach they may depend on interactions with the flow which are identified in this study for the mass transfer model by Merkle et al (1998). The linear dependencies of the Merkle model simplify the identification of these features, which are then employed to derive a simple mass transfer source term which is theoretically able to relax the flow towards equilibrium states given by a barotropic equation of state.

However, recent research by Koukouvinis & Gavaises (2015) has indicated that even with the finite mass transfer approach consistent results can be achieved by theoretically increasing the transfer rates to infinity. Employing a finite mass transfer model in an incompressible flow solver, they were able to reproduce the Riemann solution in the simulation of a shock tube problem with left-hand liquid and right-hand vapour state. The influence of mass transfer rate on both global and local flow dynamics is further investigated in combination with the effect of temporal resolution. The effect of finite mass transfer rate as discussed in this study is motivated by the so called equilibrium flow condition. Sezal (2009) defines the equilibrium flow condition by the time scale of any internal process, e.g. phase transition, being negligibly small compared to the time scale of the flow itself.

2 NUMERICAL MODEL

The open source CFD toolbox OpenFOAM (2017) is employed in the course of this study. To isolate the effect of source term magnitude on pressure dynamics, viscous effects are neglected and the Euler equation for momentum is solved:

$$\frac{\partial}{\partial t}(\rho u) + \nabla \cdot (\rho u \otimes u) = -\nabla p \tag{1}$$

With γ being the liquid volume fraction, defined as

$$\gamma = (\rho - \rho_v) / (\rho_l - \rho_v), \tag{2}$$

the cavitation model as implemented in the OpenFOAM solver interPhaseChangeFoam is represented by a source term $Cf(p, \gamma)$ in the transport equation of liquid volume fraction (Asnaghi et al 2015):

$$\frac{\partial \gamma}{\partial t} + \nabla \cdot (\gamma u) = \frac{Cf(p,\gamma)}{\rho_l} \tag{3}$$

The constant C is meant to adjust the overall magnitude of the source term, which is normalised by the liquid density ρ_l. Combining the mixture relation given by Equation (2), the volume fraction transport Equation (3) and the mass continuity equation

$$\frac{\partial \rho}{\partial t} + \underbrace{\rho \left(\nabla \cdot u \right)}_{\text{mass transfer}} + \underbrace{\left(\nabla \rho \right) \cdot u}_{\text{advection}} = 0, \tag{4}$$

and further treating the individual phases as incompressible, the local velocity divergence becomes (Asnaghi et al 2015)

$$\nabla \cdot u = kCf\left(p, \gamma\right), \qquad \text{where} \qquad k = \frac{1}{\rho_l} - \frac{1}{\rho_v}. \tag{5}$$

The model by Merkle et al (1998) is employed (see Equation (6)) in the following. For simplification, any model constant is absorbed in C_c for condensation and C_v for evaporation. The original model as implemented in OpenFOAM is slightly modified by dividing the source term by mixture density ρ. Substituting the modified Merkle source terms into mass continuity Equation (4), density cancels out from the mass transfer term, such that the mass transfer contribution to density change rate $d\rho/dt$ only depends on liquid volume fraction γ and pressure difference $p - p_v$.

$$C_{\mathrm{c,v}} f\left(p, \gamma\right) = \begin{cases} C_v \gamma \left(p - p_v\right) / \rho & \text{if} \quad p \leq p_v \\ C_c \left(1 - \gamma\right) \left(p - p_v\right) / \rho & \text{if} \quad p > p_v \end{cases} \tag{6}$$

Some results obtained from the modified Merkle model are compared to results obtained from a slightly modified Kunz model (Kunz et al 2000) as given by Equation (7). The reason for choosing the Kunz model as an alternative approach is that it suggests a substantially different condensation process.

$$C_{\mathrm{c,v}} f\left(p, \gamma\right) = \begin{cases} C_v \gamma \left(p - p_v\right) / \rho & \text{if} \quad p \leq p_v \\ C_c \gamma^2 \left(1 - \gamma\right) & \text{if} \quad p > p_v \end{cases} \tag{7}$$

The substantial difference of the Kunz model is that the condensation source term is only triggered by pressure being larger than vapour pressure, but that its magnitude does not depend on pressure. The evaporation process is exactly the same as in the modified Merkle model and also differs from the original OpenFOAM implementation by the additional term $1/\rho$ and by absorbing any model constant into C_v. The condensation term is the same as in the original OpenFOAM implementation, with model constants being absorbed into C_c.

3 EFFECT OF FINITE MASS TRANSFER

Some important effects of finite mass transfer on the phase transition behaviour can be discussed from analytical considerations. The density change per pressure change $d\rho/dp$, hence the slope of the density-pressure trajectory, is employed to illustrate the phase transition behaviour. In the following, this is exemplarily done for the evaporation process of the modified Merkle model. Substituting Equation (2) into the modified Merkle evaporation term In Equation (5) and then substituting $\nabla \cdot u$ in Equation (4) by the source term, yields the following differential equation with time dependent coefficients $a\left(t\right)$ and $b\left(t\right)$:

$$\frac{\partial \rho}{\partial t} + a\left(t\right)\rho + b\left(t\right) = 0, \tag{8}$$

where

$$a\left(t\right) = \frac{kC_v}{\rho_l - \rho_v}\left(p\left(t\right) - p_v\right)$$

and

$$b\left(t\right) = -a\left(t\right)\rho_v + \left(\rho_l - \rho_v\right)\nabla\gamma \cdot u.$$

The unknown pressure evolution $p\left(t\right)$ is approximated by a first order Taylor series expansion from p_0 at time instance t_0 and with the pressure change rate $\dot{p}$ being valid at t_0, such that

$$p\left(t\right) = p_0 + \dot{p}\left(t - t_0\right) + \mathcal{O}\left(t^2\right). \tag{9}$$

With ρ_0 being the density at time instance t_0 and $t_0 = 0$, the following expression then provides a solution of Equation (8), though in a close vicinity of t_0 only ($t \rightarrow 0$):

$$\rho\left(t\right) = \left(\rho_0 - c\left(t\right)\right) e^{-\frac{kC_v}{\rho_l - \rho_v}\left[\frac{1}{2}\dot{p}t^2 + \left(p_0 - p_v\right)t\right]} + c\left(t\right) \tag{10}$$

where

$$c\left(t\right) = \rho_v - \frac{\left(\rho_l - \rho_v\right)^2 \nabla\gamma \cdot u}{kC_v\left(\dot{p}t + p_0 - p_v\right)}$$

Solving Equation (9) for t, where $t_0 = 0$, and substituting back into Equation (10) yields a solution for ρ as a function of p for small perturbations around p_0. Further taking the pressure derivative and with $t \rightarrow t_0 \Rightarrow p \rightarrow p_0$ we get

$$\left.\frac{\partial \rho}{\partial p}\right|_{p_0} = -\frac{1}{\dot{p}}\left[kC_v\gamma\left(p_0 - p_v\right) + \left(\rho_l - \rho_v\right)\nabla\gamma \cdot u\right]. \tag{11}$$

Analogous steps for the condensation process result in

$$\left.\frac{\partial \rho}{\partial p}\right|_{p_0} = -\frac{1}{\dot{p}}\left[kC_c\left(1 - \gamma\right)\left(p_0 - p_v\right) + \left(\rho_l - \rho_v\right)\nabla\gamma \cdot u\right]. \tag{12}$$

Equations (11) and (12) represent the instantaneous slopes of the density-pressure trajectory during evaporation and condensation. It becomes evident that the slope of the density-pressure trajectory is not only proportional to the evaporation/condensation constants C_v and C_c, but also proportional to the advective density change rate $\left(\rho_l - \rho_v\right)\nabla\gamma \cdot u = \nabla\rho \cdot u$ and the reciprocal of the pressure change rate $\dot{p}$. Thus, an increase of the temporal pressure change rate has the effect of decreasing the slope of the density-pressure trajectory, thereby stretching the phase transition regime to a larger pressure range. Figure 1 depicts density-pressure trajectories for different pressure change rates, starting from the initial condition $\left(p_v, \rho_l\right)$ for evaporation (left) and $\left(p_v, \rho_v\right)$ for condensation (right), where $\rho_l = 1000$ kg/m^3, $\rho_v = 0.02$ kg/m^3 and $p_v = 2340$ Pa.

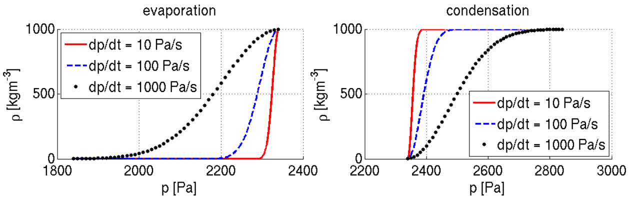

Figure 1: Density-pressure trajectories for different pressure change rates (compare to Schenke & Van Terwisga 2016)

The corresponding trajectories are obtained by numerical integration of Equations (11) and (12), respectively. In this case, advective density change is not considered, but in reality the slope of the trajectory is additionally altered by the presence of the advective term in Equations (11) and (12). The temporal density change is obtained by either taking the time derivative of Equation (10) and again employing $t \rightarrow 0 \Rightarrow p \rightarrow p_0$, or by directly substituting the mass transfer term (6) into Equation (4) and employing the relation $\gamma = (\rho - \rho_v) / (\rho_l - \rho_v)$, which gives

$$\frac{\partial \rho}{\partial t} = -kC_v \gamma (p_0 - p_v) - \nabla \rho \cdot u \tag{13}$$

for the evaporation process. Analogously, we get

$$\frac{\partial \rho}{\partial t} = -kC_c (1 - \gamma)(p_0 - p_v) - \nabla \rho \cdot u \tag{14}$$

for the condensation process.

4 A NEW MASS TRANSFER MODEL

To obtain homogeneous equilibrium states of density and pressure as given by a barotropic law, the slope of the density-pressure trajectory must follow a unique compressibility law given by a function ψ such that

$$\left.\frac{\partial \rho}{\partial p}\right|_{p_0} = \psi(\rho(p)) \quad \text{or} \quad \left.\frac{\partial \rho}{\partial p}\right|_{p_0} = \psi(p(\rho)). \tag{15}$$

For the evaporation process, the left-hand side of Equation (15) is given by Equation (11). Solving for C_v, substituting into the evaporation term of Equation (6) and then substituting the new evaporation source term into Equations (3) and (4) gives

$$\frac{\partial \gamma}{\partial t} + \nabla \cdot (\gamma u) = \frac{\rho_v}{\rho}\left[\frac{\dot{p}\psi}{\rho_l - \rho_v} + \nabla \gamma \cdot u\right] \tag{16}$$

and

$$\nabla \cdot u = -\frac{1}{\rho}\left[\dot{p}\psi + \nabla \rho \cdot u\right]. \tag{17}$$

Equations (16) and (17) represent modified transport equations of liquid volume fraction and mass. The source term establishes homogeneous equilibrium states given by the integrated compressibility law for any flow configuration. In this case, Equations (16) and (17) were derived from the evaporation process. However, starting from the condensation process yields exactly the same result. Substituting the right-hand side of Equation (17) into Equation (4), we get

$$\frac{\partial \rho}{\partial t} = \underbrace{\dot{p}\psi}_{S_\psi} + \underbrace{\nabla \rho \cdot u}_{S_{\text{adv}}^{\text{ind}}} - \underbrace{\nabla \rho \cdot u}_{S_{\text{adv}}}. \tag{18}$$

Thus, the local temporal density change can be decomposed into three sources. The term S_ψ is related to the compressibility of the flow. The other two sources cancel each other out, but formally they can be thought of as a superposition of an advective change rate S_{adv} and an advective change rate induced by phase transition $S_{\text{adv}}^{\text{ind}}$, such that the mass transfer contribution is given by

$$S_{\text{MT}} = S_\psi + S_{\text{adv}}^{\text{ind}}. \tag{19}$$

The overall density change resulting from Equation (18) is interpreted as the time derivative of the barotropic law:

$$\frac{\partial}{\partial t}\left[\rho(p(t))\right] = \frac{\partial \rho}{\partial p}\frac{\partial p}{\partial t} = \psi \dot{p} \tag{20}$$

In fact, substituting Equation (20) into Equation (4) and solving for $\nabla \cdot u$ directly yields Equation (17). In case of a divergence free two-phase flow, Equation (17) implies that S_ψ and $S_{\text{adv}}^{\text{ind}}$ cancel out of Equation (18) and the local density change is only driven by advection then. In contrast to the density change through finite mass transfer given by Equations (13) and (14), density change is now given by a single function, which depends on pressure change rate instead of pressure differences and includes a counterpart to the advective change rate. In addition, the density change behaviour can now be adjusted by the choice of the compressibility law for ψ. To demonstrate the capability of the modified mass transfer model given by Equations (16) and (17), the following barotropic equation of state is employed to model the compressibility of the flow (see Koop et al 2006):

$$\rho(p) = \frac{\rho_l}{2}\left[1 + \frac{\rho_v}{\rho_l} + \left(1 - \frac{\rho_v}{\rho_l}\right)\tanh\left(\frac{2(p - p_v)}{(\rho_l - \rho_v)c_{\text{min}}^2}\right)\right] \tag{21}$$

Note that in this case p_v denotes the pressure associated with the minimum speed of sound of the barotropic law. With c_{min} being the corresponding minimum speed of sound in the mixture regime, the compressibility law as a function of ρ is then given by

$$\psi(\rho) = \left(\frac{2}{(\rho_l - \rho_v)c_{\text{min}}}\right)^2 (\rho - \rho_v)(\rho_l - \rho). \tag{22}$$

The constants ρ_l and ρ_v denote the incompressible limit states of Equation (22). For this study, they are arbitrarily chosen to be $\rho_l = 1000$ kg/m^3 and $\rho_v = 0.02$ kg/m^3. The minimum speed of sound is arbitrarily assumed to be $c_{\text{min}} = 0.5$ m/s. The equilibrium mass transfer model is applied to the following, strongly simplifying situation. Imposing artificial signals of $p(t)$ and u and numerically integrating Equation (18) with a first order scheme

$$p(t + \Delta t) = p(t) + \dot{p}(t)\Delta t \tag{23}$$

yields a solution for the density pressure trajectory. In case of a density jump as it would occur across the interface of a bubble, the density gradient becomes a numerical artifact because it approaches infinity with increasing spatial resolution. For this study, the density gradient is assumed to be related to a one dimensional control volume size Δx as follows:

$$\nabla \rho = \frac{\rho - \rho_v}{\Delta x} \tag{24}$$

The test case is now considered to be a one dimensional control volume, which is initially fully occupied by water. The compressibility model required as an input of the source term is given by Equation (22) and the corresponding equation of state is given by Equation (21). An evaporation process with subsequent condensation and with non-constant pressure change is considered. The pressure signal is given by a standard distribution stretched by constant a and shifted to the level of initial pressure by constant p_0:

$$p\left(t\right) = \frac{a}{\sqrt{2\pi}\sigma} e^{-\frac{1}{2}\left(\frac{t-\mu}{\sigma}\right)^2} + p_0 \qquad (25)$$

With $a < 0$, the pressure signal given by Equation (25) is associated with evaporation until $t = \mu$. From this time instant on, the sign switch of the pressure change rate $\dot{p}$ causes condensation. It is required that the overall process shall cover a pressure range $\Delta p = p_T - p_0$, where p_0 is the pressure at time instance $t = 0$ and p_T the pressure at $t = T$. Thus, we get

$$p\left(t = \mu\right) = \Delta p \qquad \Rightarrow \qquad a = \Delta p \sqrt{2\pi}\sigma. \qquad (26)$$

It is assumed that $\mu = T/2$ and $\sigma = T/8$. The pressure time derivative reads as follows:

$$\dot{p}\left(t\right) = -\frac{a\left(t-\mu\right)}{\sqrt{2\pi}\sigma^3} e^{-\frac{1}{2}\left(\frac{t-\mu}{\sigma}\right)^2} \qquad (27)$$

With $\Delta t = T - t_0 = 20$ s, $p\left(t\right)$ and $\dot{p}\left(t\right)$ evolve as depicted by Figure 2.

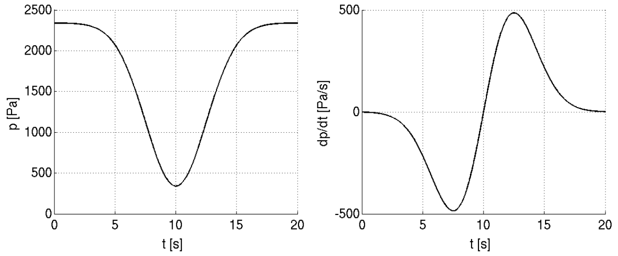

Figure 2: Pressure (left) and pressure time derivative signal (right)

In a first case, advective density change is neglected. The evolution of the individual density change contributions in Equations (18) and (19) are depicted in Figure 3. The temporal density evolution is only driven by the compressibility term S_ψ. The corresponding density-pressure trajectory is given by the blue dotted curve in Figure 5 (left). The barotropic curve given by Equation (21) is represented by the red solid line. Starting from liquid density, the trajectory computed from the equilibrium mass transfer model first follows the barotropic curve in direction of decreasing pressure, which corresponds to the negative density change in Figure 2. It then turns around in the vapour regime due to the sign switch of the $\dot{p}$ signal (see Figure 2 right) and follows the barotropic curve back to the starting point.

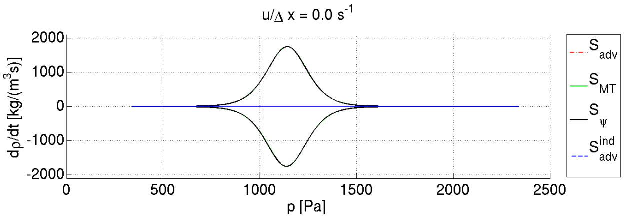

Figure 3: Contributions to density change from Equation (18) without advective density change

In a second case, advective density change is included, where $u/\Delta x = 0.5\ \mathrm{s}^{-1}$. From Equation (18) follows that a positve density gradient in combination with a positive velocity has a tendency to decrease the local density as represented by the red dashed S_adv curve in Figure 4. In the non-cavitating liquid regime, however, the equation of state requires that density must be almost constant. This implies that a counterpart to the advective density change must exist, which is given by the source term induced advection $S^\mathrm{ind}_\mathrm{adv}$ (see blue dashed line in Figure 4). As evaporation starts, the advective density change rates decrease due to Equation (24). As the trajectory follows the barotropic state curve in opposite direction again, they increase during condensation accordingly. Note that the overall source term induced change rate S_MT as given by Equation (19) is smaller during the evaporation process in this case. This is because the advective density change rate S_adv works in the same direction as S_ψ during evaporation in this case. In that sense, the overall source term induced change rate S_MT can be seen as the rate of relaxation at which density is temporarily driven to the equilibrium state.

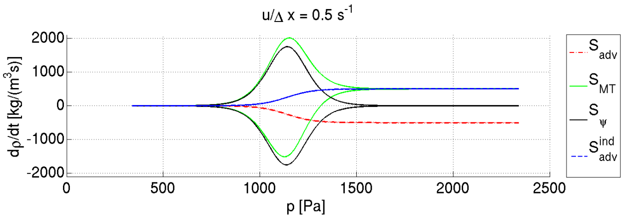

Figure 4: Contributions to density change from Equation (18) with advective density change

In both cases, the density-pressure trajectory obtained from the equilibrium mass transfer model follows the barotropic reference curve. Small deviations occur which are a result of the time discretisation errors. In this case, time step size in Equation (23) is $\Delta t = 10^{-3}$ s.

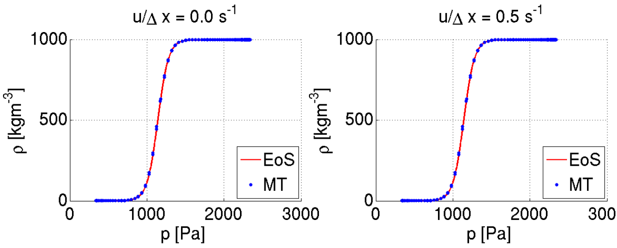

Figure 5: Density-pressure trajectories (MT) corresponding to Figures 3 and 4 and barotropic equation of state (EoS)

5 SINGLE BUBBLE COLLAPSE

In the following, the slightly modified Merkle mass transfer model given by Equation (6) is applied to a single bubble collapse. Effects of finite mass transfer on the evolution of density-pressure trajectories are studied and qualitatively compared to the characteristics predicted by Equation (12).

In addition, a convergence study on local peak quantities with respect to mass transfer rate and temporal resolution is carried out.

5.1 Numerical Set-Up of the Bubble Case

The initial bubble radius is $R_0 = 0.4$ mm and the initial radial pressure distribution, depicted in Figure 6, satisfies the Laplace equation as found in (Franc & Michel 2004), where the interior pressure is $p_v = 2340$ Pa. More details on the numerical set-up are found in (Schenke & Van Terwisga 2016). Analytical reference solutions are obtained from the Rayleigh-Plesset equation in the absence of viscous forces and surface tension (Franc & Michel 2004).

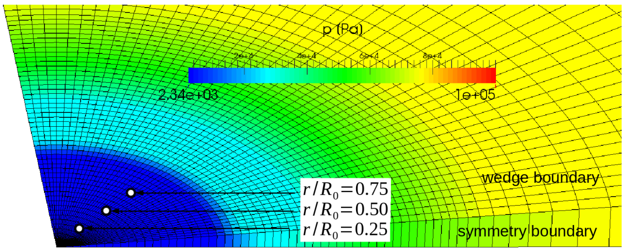

Figure 6: Computational grid and initial pressure field (Schenke & Van Terwisga 2016)

5.2 Results of the Bubble Case

Figure 7 depicts curves of radius evolution for three different condensation rates and three different time step sizes.

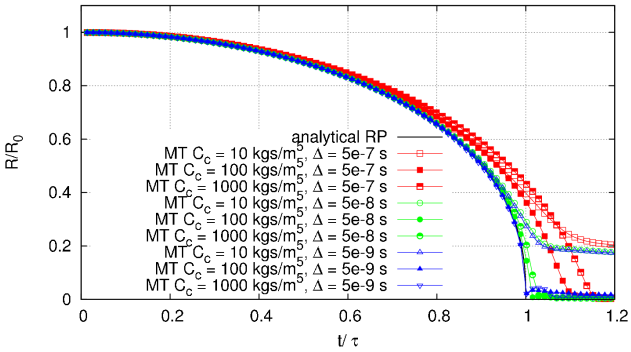

Figure 7: Evolution of the bubble radius R for different condensation rates and time step sizes (compare to Schenke & Van Terwisga 2016)

In this case the medium condensation rate $C_c = 100$ kgs/m^5 is associated with the smallest collapse time. Both the larger rate $C_c = 1000$ kgs/m^5 and the smaller rate $C_c = 10$ kgs/m^5 result in larger collapse times for all time step sizes, where the latter goes along with a sudden deceleration of bubble radius decay at around $R/R_0 = 0.2$. As already shown by Schenke & Van Terwisga (2016), this situation goes along with a very pronounced interface diffusivity. This causes a pronounced bulk flow across the theoretically sharp interface, thereby forming a stagnation point at the bubble centre due to the symmetry of the flow. The local peak pressure may then dissolve into the domain before vapour is fully destroyed, thereby decreasing the magnitude of the local mass transfer source term drastically. The only effective means to approach the analytical Rayleigh collapse time τ is to keep the mass transfer rate large and to provide sufficient temporal resolution at the same time. As time step size is decreased, the R/R_0-curves collapse on the curve obtained from the analytical solution, given that the condensation rate is sufficiently large.

The dependency between condensation rate and steepness of the density-pressure trajectory as predicted by Equation (12) is qualitatively confirmed by Figure 8, which depicts the density trajectories at the observation points in Figure 6 for different time step sizes and condensation rates. As the bubble centre is approached, the local pressure change is getting more rapid. Since the slope of the density-pressure trajectory of the modified Merkle model is proportional to $1/\dot{p}$, the slope is supposed to decrease as the bubble centre is approached. While being highly dependent on mass transfer rate, the slopes of density-pressure trajectories are hardly time step size dependent. The horizontal parts of the trajectories result from the rebound event. They evolve horizontally as long as pressure is above vapour pressure.

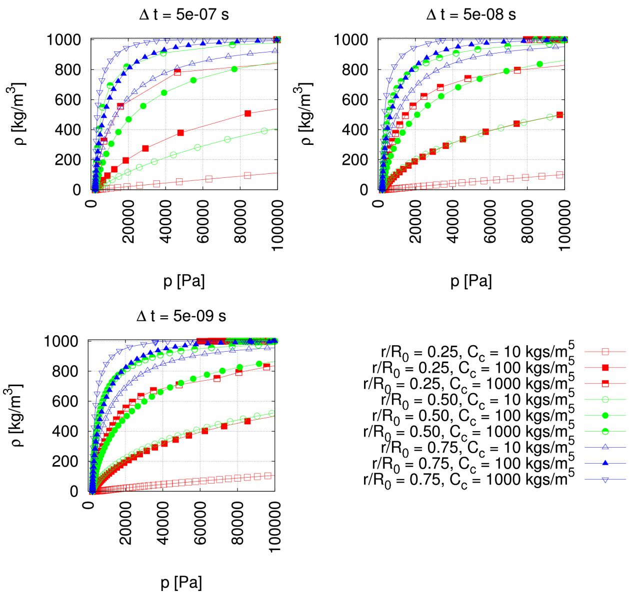

Figure 8: ρ-p trajectories at the observation points indicated in Figure 6 for different condensation rates and time step sizes (compare to Schenke & Van Terwisga 2016)

The effect of time step size on transient phase transition behaviour is analysed by evaluating the temporal density change rate $d\rho/dt$ at observation point $r/R_0 = 0.25$ indicated in Figure 6. Figure 9 depicts $d\rho/dt$ signals for constant condensation rate and variable time step size. It shows that sufficient temporal resolution is needed to focus the local phase transition time to small intervals.

To further investigate the influence of mass transfer rate and temporal resolution on peak events, a convergence study of the local phase transition rate with respect to condensation rate and time step size is carried out. Figure 10 depicts the evolution of the $d\rho/dt$ peak value over condensation rate and for three different time step sizes and at the three different observation points indicated in Figure 6. It becomes clearly evident that the local phase transition speed exhibits convergent behaviour with increasing condensation rate and a fixed time step size. Figure 10 and also Figure 9 further indicate convergent behaviour of the local phase transition speed with increasing temporal resolution.

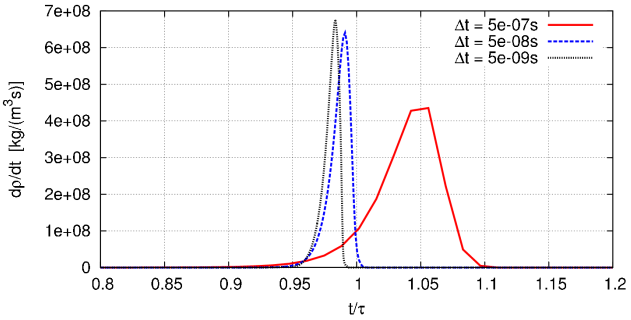

Figure 9: Evolution of $d\rho/dt$ at $r/R_0 = 0.25$ for $C_c = 250$ kgs/m^5 and different time step sizes

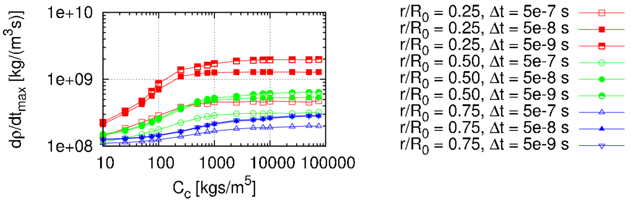

Figure 10: $d\rho/dt$ peak over condensation rate at different observation points and for different time step sizes

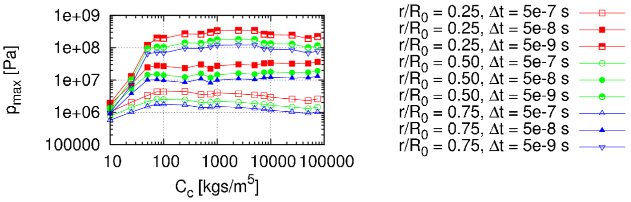

Figure 11: Peak pressure over condensation rate at different observation points and for different time step sizes

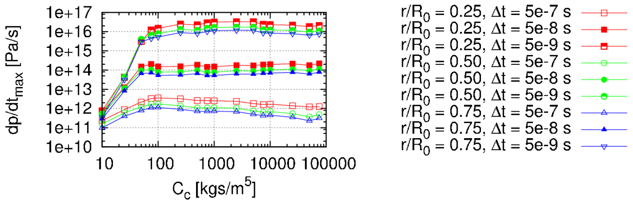

Figure 12: dp/dt peak over condensation rate at different observation points and for different time step sizes

The same convergence study is applied to peak pressures (see Figure 11) and peak pressure time derivatives (see Figure 12) at the observation points indicated in Figure 6. Similar to the peak of local density change rate, both quantities exhibit convergent behaviour with respect to condensation rate. However, there is no indication of time step size convergence observed, implying that the magnitude of peak pressures is not reliably predicted.

6 CAVITATING WEDGE FLOW

The effect of finite mass transfer rate and temporal resolution on cavitating flow dynamics is further investigated for a wedge flow. In the following, both the slightly modified Merkle model and the slightly modified Kunz model given by Equations (6) and (7) is employed.

6.1 Numerical Set-Up of the Wedge Case

Geometry (see Figure 13), ambient pressure and mean flow velocity for the wedge study are in line with a simulation carried out by Budich et al (2015), using the fully compressible Riemann-solver CATUM to solve the compressible Euler equations. Budich et al (2015) employed a barotropic equation of state assuming equilibrium speed of sound in the mixture regime. Originally, this configuration was investigated experimentally by Ganesh (2015). The inlet boundary condition is given by a uniform inflow speed of 8.0 m/s. The outflow passes a diffuser to avoid the reflection of pressure disturbances at the outlet, where the pressure boundary condition is imposed.

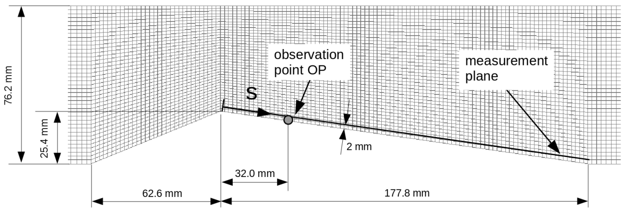

Figure 13: Geometry and computational grid

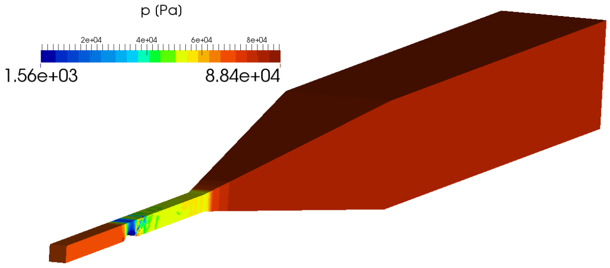

Figure 14: Computational domain and instantaneous pressure field

Figure 14 depicts the instantaneous pressure field under cavitating flow conditions. The outlet pressure is set such that the pressure downstream from the wedge approximately matches 52 kPa as reported by Ganesh (2015). The required diffuser outlet pressure was determined by Bernoulli's equation in combination with the mass continuity equation, which is valid due to the neglect of viscous forces. However, energy is not explicitly conserved here, which leads to a certain offset of the pressure downstream from the wedge. Under wetted flow conditions, the required pressure was overestimated by 0.88 kPa. Both liquid density ρ_l and vapour density ρ_v were evaluated at the targeted downstream pressure of 52 kPa and an ambient temperature of 293.15 K. A characteristic cell size of 2 mm in the vicinity of the wedge turned out to be sufficient to get a converged shedding frequency. Due to the neglect of viscous forces, top, bottom and side walls are treated as slip walls. For the modified Merkle model (see Equation (6)), the evaporation constant C_v was increased until pressure was prevented from dropping below vapour pressure p_v significantly, which gave $C_v = 100$ kgs/m^5. The condensation constant was increased until no significant pressure increases at low densities was observed during condensation, which gave $C_c = 200$ kgs/m^5. The evaporation term of the modified Kunz model is exactly the same as in the modified Merkle model. Applying the same strategy to identify an appropriate value for the condensation constant of the Kunz model resulted in $C_c = 1000$ kg/(sm^3).

6.2 Results of the Wedge Case

The ρ-p trajectories obtained from the modified Merkle and Kunz models, measured at observation point OP indicated in Figure 13, are depicted in Figure 15. It becomes apparent that especially the modified Merkle model exhibits a physical behaviour in the sense that pressure remains close to vapour pressure in the mixture regime, except for the final stage of local condensation. It is generally observed that the slope of the ρ-p trajectory obtained from the modified Merkle model tends to be much larger during evaporation than during condensation. The difference is explained by the dependency of the trajectory slope on the reciprocal of the pressure time derivative $\dot{p}$ (see Equation (12)), whose magnitude can get very large during cavity collapses. Again, no significant influence of time step size on the shape of the trajectories is observed. It is further observed that the slope of the condensation trajectory obtained from the Kunz model is even steeper at large densities, but that it exhibits rather non-physical pressure fluctuations at small densities.

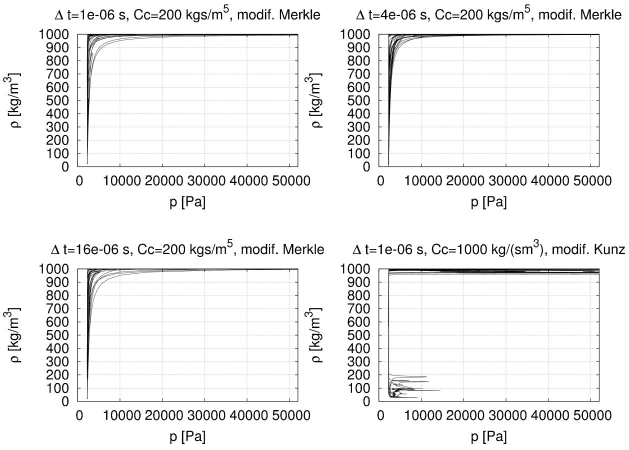

Figure 15: ρ-p trajectories at the observation point in Figure 13 obtained from the modified Merkle model (three different time step sizes) and the modified Kunz model

Shedding frequencies are compared with each other by means of a s-t diagram. The s-t diagram depicts the spanwise averaged volume fraction in a measurement plane parallel at 2 mm distance from the wedge surface (see Figure 13) over time. Figure 16 depicts the results obtained from the modified Merkle and Kunz model, respectively. Although the volume fraction transport Equation (3) is based on liquid volume fraction, Figure 16 depicts the vapour volume fraction for better comparability to the results of Ganesh (2015) and Budich et al (2015). For the smallest time step size $\Delta t = 10^{-6}$ s, both the modified Merkle and Kunz model yield slightly smaller shedding frequencies and overestimation of overall vapour content compared to the results by Budich et al (2015). It is observed that temporal resolution significantly affects the global shedding behaviour. As seen in the s-t diagram for the largest time step size $\Delta t = 16 \cdot 10^{-6}$, large mass transfer rates in combination with large time steps result in massive overestimation of vapour volume and underestimation of shedding frequency. For $\Delta t = 10^{-6}$, the shedding frequencies obtained from the modified Merkle model were found to be converged. Similar to the cavity shedding frequency, the frequency of local pressure impacts at observation point OP obtained from the modified Merkle and the Kunz model (see Figure 17) is in good agreement with the frequency reported by Ganesh (2015) for the smallest time step size. Ganesh (2015) measured 19 events per second, which is equal to 5.5 events per 0.29 seconds. The same time step size dependency as in the s-t-diagrams is observed for the modified Merkle model. Taking the wiggles of the ρ-p trajectory in the low density regime as seen in Figure 15 into account, some peaks up to a magnitude of 15000 Pa obtained from the Kunz model are considered as non-physical. The rapidness of the local pressure signals decreases with increasing time step size.

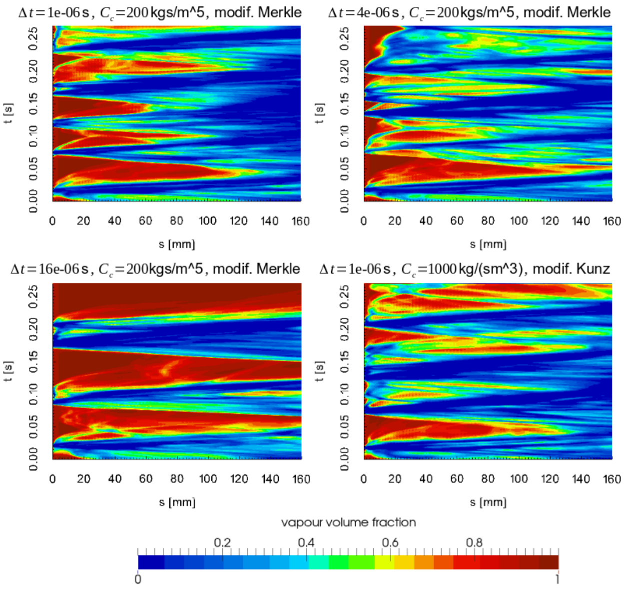

Figure 16: s-t diagrams measured in the plane indicated in Figure 13 obtained from the modified Merkle model (three different time step sizes) and the modified Kunz model

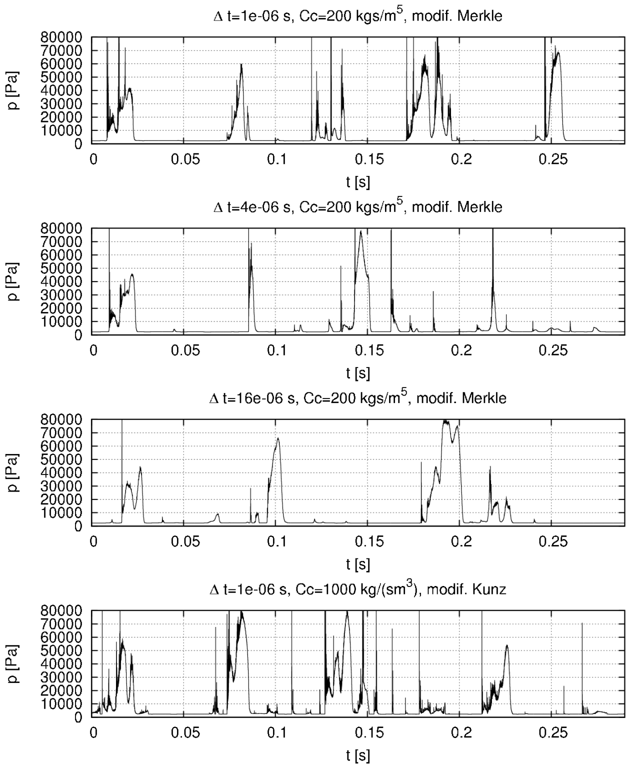

Figure 17: Pressure evolution at the observation point in Figure 13 obtained from the modified Merkle model (three different time step sizes) and the modified Kunz model

It should be mentioned that the underestimation of shedding frequency and overestimation of vapour content for large time steps can be avoided by decreasing the condensation rate. Figure 18 depicts the s-t and ρ-p diagram obtained from the modified Merkle model with the largest time step size, but with the condensation rate being decreased by a factor of 200 compared to Figures 15 and 16. The evaporation rate is still $C_v = 100$ kgs/m^5. However, results obtained from this configuration are extremely sensitive to variation of condensation rate. Furthermore, the density-pressure coupling appears to be non-physical. Decreasing the evaporation rate as well would eventually result in the prediction of negative pressures. Figure 19 shows that the local pressure signals are smoothened as a result of insufficient temporal resolution in combination with small condensation rates.

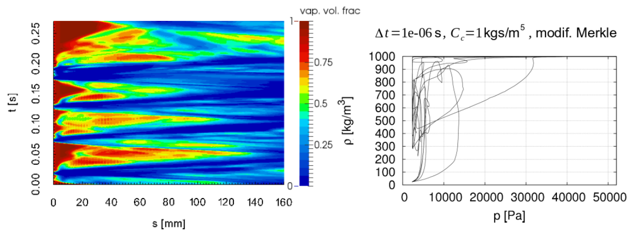

Figure 18: s-t diagram (left) and ρ-p trajectory (right) at the observation point in Figure 13 obtained from the modified Merkle model with large time step size and small condensation rate

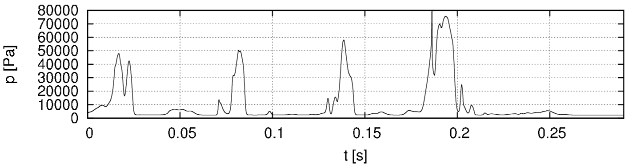

Figure 19: Pressure evolution at the observation point in Figure 13 obtained from the modified Merkle model with $\Delta t = 16 \cdot 10^{-6}$ s and $C_c = 1$ kgs/m^5

Especially for the modified Merkle model, similar shedding mechanisms as reported by Ganesh (2015) and Budich et al (2015) are observed. The collapse phase is at least partially associated with a condensation discontinuity travelling upstream. Figure 20 indicates the formation of a left-hand/right-hand side state at the sheet closure, identified by a jump of both axial velocity and volume fraction across the condensation front at the closure region. Different from a re-entrant jet mechanism, the flow right from the cavity closure is heading backward across the whole height of the closure region. The same was found by Budich et al (2015).

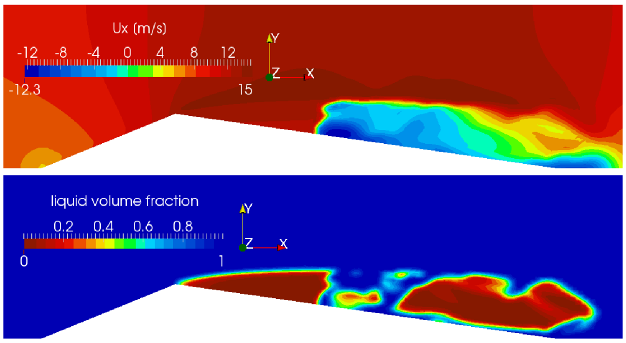

Figure 20: Instantaneous axial velocity field (above) and volume fraction field (below) at the centre plane at $t = 0.066$ s obtained from the modified Merkle model with $\Delta t = 10^{-6}$ s and $C_c = 200$ kgs/m^5

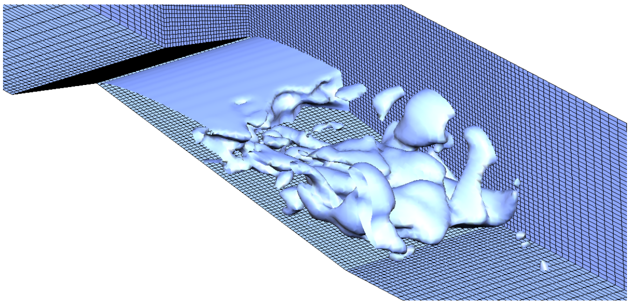

Figure 21: Instantaneous vapour structures ($\gamma \leq 0.5$) at $t = 0.066$ s obtained from the modified Merkle model with $\Delta t = 10^{-6}$ s and $C_c = 200$ kgs/m^5

Figure 21 depicts the instantaneous three dimensional vapour structures at the same time instance, also indicating the formation of a condensation front rather than a thin re-entering liquid jet. However, it should be noted that the re-entrant jet mechanism has been observed as well in this simulation and that it appears to be difficult to always clearly distinguish those two effects.

CONCLUSIONS & RECOMMENDATIONS

It has been shown that the finite mass transfer approach incorporated in an incompressible CFD solver is able to reflect the density-pressure coupling in the cavitating flow regime to a satisfactory extent. In order to obtain realistic density-pressure coupling, the equilibrium flow condition (Sezal 2009) must be approached, which requires large mass transfer rates. Similar conclusions have been drawn by Koukouvinis & Gavaises (2015) and Bhatt et al (2015). Increasing the mass transfer rate goes along with a tendency to focus the local phase transition to small time intervals, which requires sufficient temporal resolution within those time intervals. This suggests that the required temporal resolution is governed by the collapse time of characteristic cavities resolved by the simulation rather than the Courant number. Distribution and steepness of the density-pressure trajectory is an indicator of the closeness to the equilibrium flow condition. With the mass transfer rate being sufficiently large, the slope of the density-pressure trajectory locally mimics the mixture compressibility as given by more realistic barotropic equations of state, although the density-pressure states of the flow are still not unique. An alternative mass transfer approach that is theoretically able to relax the flow towards homogeneous equilibrium states given by an arbitrary barotropic equation of state has been suggested. The applicability of this approach in the pressure-based numerical framework will be further investigated.

ACKNOWLEDGMENTS

Financial support of this research is provided by the EU CaFE ITN initiative and the MARIN Academy. We also thank Dr. Steffen Schmidt (TU Munich), Prof. Rickard E. Bensow (Chalmers University of Technology) and the further members of the CaFE ITN project for the inspiring discussions on numerical modelling of cavitation, as well as Dr. Duncan R. van der Heul and Prof. Gijs Ooms (TU Delft) for their helpful feedback on the ongoing research. We further greatly appreciate the fruitful cooperation with Mohammad H. Khanouki and Ebrahim Ghahramani (Chalmers University of Technology), who have, amongst others, kindly shared the mesh for the bubble collapse test case.

REFERENCES

Asnaghi, A., Feymark, A. & Bensow, R.E. (2015). 'Numerical Simulation of Cavitating Flows Using OpenFOAM'. Proceedings of the 18th Numerical Towing Tank Symposium, Cortona, Italy.

Bhatt, M., Gnanaskandan, A. & Mahesh, K. (2015). 'Evaluation of finite rate homogenous mixture model in cavitation bubble collapse'. Proceedings of the 9th International Symposium on Cavitation, Lausanne, Switzerland.

Budich, B., Neuner, S., Schmidt, S.J. & Adams, N.A. (2015). 'Numerical investigation of shedding partial cavities over a sharp wedge'. Proceedings of the 9th International Symposium on Cavitation, Lausanne, Switzerland.

Charrière, B., Decaix, J. & Goncalvès , E. (2015). 'A comparative study of cavitation models in a Venturi flow'. European Journal of Mechanics B/Fluids **49**(2015), pp. 287–297.

Franc, J.-P. & Michel, J.-M. (2004). Fundamentals of Cavitation. Kluwer Academic Publishers.

Frikha, S., Coutier-Delgosha, O. & Astolfi, J.A. (2008). 'Influence of the Cavitation Model on the Simulation of Cloud Cavitation on 2D Foil Section'. International Journal of Rotating Machinery 2008.

Ganesh, H. (2015) 'Bubbly Shock Propagation as a Cause of Sheet to Cloud Transition of Partial Cavitation and Stationary Cavitation Bubbles Forming on a Delta Wing Vortex'. PhD thesis, University of Michigan.

Koop, A.H., Hoeijmakers, H.W.M., Schnerr, G.H. & Foeth, E.J. (2006). 'Design of Twisted Cavitating Hydrofoil Using a Barotropic Flow Method'. Proceedings of the 6th International Symposium on Cavitation, Wageningen, The Netherlands.

Koukouvinis, P. & Gavaises, M. (2015). 'Simulation of throttle flow with two phase and single phase homogenous equilibrium model'. Proceedings of the 9th International Symposium on Cavitation, Lausanne, Switzerland.

Kunz, R.F., Boger, D.A., Stinebring, D.R., Chyczewski, T.S., Lindau, J.W., Gibeling, H.J., Venkateswaran, S. & Govindan, T.R. (2000). 'A preconditioned Navier-Stokes method for two-phase flows with application to cavitation prediction'. Computers and Fluids **29**(8), pp. 849–875.

Merkle, C.L., Feng, J.Z. & Buelow, P.E.O. (1998). 'Computational modeling of the dynamics of sheet cavitation'. Proceedings of the 3rd International Symposium on Cavitation, Grenoble, France.

OpenFOAM (2017), OpenFOAM web site, 2017.

Schenke, S. & van Terwisga, T.J.C. (2016). 'Finite Mass Transfer Effects in Cavitation Modelling'. Proceedings of the 19th Numerical Towing Tank Symposium, St Pierre d'Oléron, France.

Sezal, I.H. (2009) 'Compressible Dynamics of Cavitating 3-D Multi-Phase Flows'. Dissertation, Technische Universität München.